

RESEARCH ARTICLE | JANUARY 16 2024

A comparative study on transport and interfacial physics of $H_2/CO_2/CH_4$ interacting with H_2O and/or silica by molecular dynamics simulation

Cheng Chen (陈斌) ; Jun Xia (夏钧)  

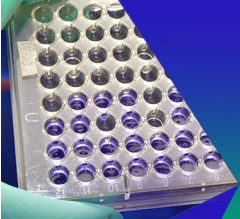


Physics of Fluids 36, 016606 (2024)


<https://doi.org/10.1063/5.0184754>



CrossMark



Biomicrofluidics
Special Topic:
Microfluidics and Nanofluidics in **India**
Submit Today



A comparative study on transport and interfacial physics of H₂/CO₂/CH₄ interacting with H₂O and/or silica by molecular dynamics simulation

Cite as: Phys. Fluids **36**, 016606 (2024); doi: 10.1063/5.0184754

Submitted: 26 October 2023 · Accepted: 19 December 2023 ·

Published Online: 16 January 2024



View Online



Export Citation



CrossMark

Cheng Chen (陈斌),  and Jun Xia (夏钧)^{a)} 

AFFILIATIONS

Department of Mechanical and Aerospace Engineering, and Institute of Energy Futures, Brunel University London, Uxbridge UB8 3PH, United Kingdom

^{a)} Author to whom correspondence should be addressed: jun.xia@brunel.ac.uk

ABSTRACT

Underground H₂ storage (UHS), i.e., injecting H₂ into subsurface geological formation and its withdrawal when needed, is identified as a promising solution for large-scale and long-term storage of H₂. In this study, molecular dynamics (MD) simulation was performed at a typical temperature 320 K with pressure up to 60 MPa to predict H₂ transport properties and H₂-H₂O-rock interfacial properties, which are compared with those of CO₂ and CH₄. The MD results show that the CH₄ profiles of property variations with pressure lie between those of H₂ and CO₂ and more comparable to CO₂. The interaction of H₂ with H₂O/silica is much weaker than that of CH₄ and CO₂. It is found that the effect of H₂ pressure on altering the water contact angle and interfacial tension is negligible under all conditions. Unlike the multi-adsorption layers of the confined CO₂ and CH₄, there is only one adsorption layer of H₂ confined by silica nano-slit. The planar diffusion of H₂ in the confined system is slower than that in the bulk system at pressures lower than 20 MPa. The data and findings of this study will be useful for modeling the multiphase flow dynamics of UHS on reservoir scale, optimizing UHS operation, and assessing the performance of a cushion gas, e.g., CO₂ or CH₄.

© 2024 Author(s). All article content, except where otherwise noted, is licensed under a Creative Commons Attribution (CC BY) license (<http://creativecommons.org/licenses/by/4.0/>). <https://doi.org/10.1063/5.0184754>

I. INTRODUCTION

Hydrogen is attracting enormous attention because it is identified as a zero-carbon energy carrier, which will play a key role in achieving net-zero emissions. H₂ has notable advantages such as a high energy density (141.86 MJ/kg, 2–3 times higher than most hydrocarbon fuels¹) and, more importantly, clean products in combustion that can contribute significantly to decarbonize transportation, domestic heating, and power generation. Although 95% of H₂ in the market is still produced from fossil fuels such as the steam reforming of natural gas,² green H₂ produced by water electrolysis using renewable energy like solar/wind scales up rapidly in recent years. It is estimated that the production of low-emission H₂ could reach 16–24 × 10⁶ tons per year, with 9–14 × 10⁶ tons based on electrolysis by 2030.³

The storage of H₂ remains a major barrier on the deployment of green H₂ because the conventional surface storage facilities (e.g., high-pressure tanks) cannot meet the requirements of the capacity and time span on the scales of GW h–TW h and weeks/months, respectively, considering the fluctuation of H₂ production due to the intrinsic

intermittency of the renewable energy and the inter-seasonal discrepancies of demands (e.g., intensified demand for heat in winter).^{4,5} Subsurface H₂ storage in geological formations of salt caverns, saline aquifers, and depleted oil/gas fields, i.e., the so-called underground H₂ storage (UHS), emerges as a promising method to achieve large-scale and long-term H₂ storage. It has been proven that UHS in salt caverns is commercially feasible by an industrial-scale project (a mixture of 95% H₂ and 3%–4% CO₂) implemented in Teesside, UK,⁶ whereas the progress is slow on UHS in depleted gas fields and aquifers. Salt caverns are impermeable while the other reservoirs feature porous media.

Injection of H₂ into porous reservoirs displaces the original fluids, leading to complex multiphase flow processes controlled by rock properties (e.g., permeability and porosity), fluid properties (e.g., density, viscosity, and diffusivity), and fluid–rock interfacial properties [e.g., wettability, interfacial tension (IFT), and surface adsorption].^{4,6} During injection/withdrawal cycles, cushion gas such as CH₄ or CO₂ is needed to work as a buffer to maintain the pressure (for H₂ extraction at a desired pressure and flow rate), prevent water from entering the stored compartment, and optimize storage spaces.^{7,8}

In some aspects, UHS is comparable with other underground gas storage (UGS) of town gas and nature gas, as both involve compressed gases being injected, stored, and withdrawn cyclically in subsurface formations. It should be noted that UHS and UGS are different from CO₂ geo-storage (CGS) in which there is no withdrawal or extraction process, and the dissolution and mineralization processes are regarded as the most secured CO₂ trapping mechanisms. The dissolution and geochemical reactions of H₂ would be clearly unfavorable in UHS scenarios, on the other hand. Previous extensive experiences in UGS and CGS can provide useful guides for UHS. It is, however, emphasized by Pan *et al.*^{9,10} that direct extrapolation from these different scenarios should be avoided given that fundamental properties of H₂ are significantly different from those of CO₂ and CH₄, as shown in Table I. For example, H₂ has a much higher diffusivity, lower solubility/density/viscosity than CH₄ and CO₂. H₂/CO₂/CH₄ can switch between a gas phase and supercritical fluid at underground conditions. Meanwhile, CO₂ is also likely to exist in liquid phase owing to its high critical temperature of 304.13 K. It is also found that UHS and CGS exhibit significant differences in gas saturation distribution due to their differences of gas–brine relative permeability hysteresis.¹⁰ Therefore, the transport and interfacial properties of H₂/CO₂/CH₄ interacting with H₂O and/or rock over a wide range of operating conditions should be comprehensively investigated and compared to better understand their differences in hydrodynamics and trapping mechanisms. Reliable property data are a precondition to reducing the uncertainties in site selection and cushion gas assessment, guiding future pilot and industrial-scale UHS projects.

As critically reviewed by Aslannezhad *et al.*,¹¹ a few experimental measurements were carried out recently to investigate the effects of temperature, pressure, fluid properties (gases, salinity, ion types, organic acids, etc.), and rock properties such as the surface chemistry and roughness on the contact angle (CA) and interfacial tension for H₂–brine–rock systems. CA is a quantitative measure of the wetting of a solid by a liquid, and IFT measures the force holding the surface of a particular phase together, which are both important in determining the physics of H₂ flow in porous media and hydrodynamics such as rock–fluid and fluid–fluid interactions.^{12–14} Moreover, the injected gases would migrate upwards due to buoyancy until reaching the caprock, which is referred to as structural trapping.⁴ The interfacial interaction among the gas, water, and rock also affects the storage safety and capacity as it determines the capillary entry pressure (P_c) and the maximum column height (h) of the gases sealed beneath the cap-rock.¹⁵

TABLE I. Molecular and thermophysical properties of H₂, CO₂, CH₄, and H₂O at 25 °C and 1 atm.²²

Properties	H ₂	CO ₂	CH ₄	H ₂ O
Molecular weight (g/mol)	2.02	16.04	44.09	18.02
Dipole moment (Debye)	0.0	0.0	0.0	1.86
Boiling temperature (K)	20.37	194.69	111.67	373.12
Critical temperature (K)	33.15	304.13	190.56	647.10
Critical pressure (MPa)	1.30	7.38	4.60	22.06
Density (kg/m ⁻³)	0.089	1.98	0.657	997.05
Viscosity (μPa s)	8.90	14.914	11.076	890.02
Solubility in pure water (g/l)	16 × 10 ⁻⁶	1.45 × 10 ⁻³	22.7 × 10 ⁻³	...

$$P_c = \frac{2\gamma_{gw} \cos \theta}{R} = \Delta\rho gh, \quad (1)$$

where γ_{gw} is the interfacial tension between the gas and water, θ is the contact angle, R is the pore through radius, $\Delta\rho$ is the gas–water density difference, and g is the gravitational constant.

The data available for H₂ are still sparse compared to CO₂ and CH₄. The wide variability and considerable inconsistencies for the measured contact angle in reported data of CO₂ and CH₄^{15–20} suggest that more elaborated experimental measurements (e.g., effective surface preparation, standard protocol for sample processing, distinguishing artificial contamination using advanced imaging techniques^{18,19}) of H₂–brine–rock systems are needed to reduce the uncertainty. Another property that is rather challenging to be experimentally measured but urgently needed is the surface adsorption and diffusivity of H₂ in reservoir pores, particularly the nanopores of 5–15 nm,²¹ as the physical properties of gases may change dramatically due to the nanoconfinement.

Modeling methods at molecular scales such as molecular dynamics (MD) simulation provide a cost-effective and safe means of studying multiphase systems composed of hazardous substances under extreme conditions. Its capability of reducing experimental uncertainties and avoiding logistical challenges associated with flammable gases under high-temperature, high-pressure conditions makes it a valuable tool for UHS research and exploration. MD simulation has been used extensively to study CO₂/CH₄–brine–rock systems and predict interfacial properties of the wettability,^{23–26} IFT,^{27–31} surface adsorption, and nanoconfined diffusion^{32–36} for the applications of CGS or CO₂ enhanced shale gas recovery. This study is motivated by the lack of H₂ property data in realistic reservoir conditions and understanding of the differences in properties as H₂/CO₂/CH₄ interacts with brine and/or rock. The novelty of the present study, therefore, lies in using molecular dynamics simulation to provide these important missing parameters under typical under-surface porous-reservoir conditions.

To this end, MD simulation was performed to predict and compare the properties of H₂/CO₂/CH₄–H₂O–silica systems at 320 K and pressure up to 60 MPa (the pressure can be higher than 30 MPa in the context of UHS¹¹). The paper is organized as follows: Details of the molecular models, force fields, system configuration, and MD setups are given in Sec. II. Results of the effects of gas pressure on transport properties in the bulk phase, and interfacial properties of wettability, surface tension, surface adsorption, and the diffusion coefficient of gas–water–silica multiphase systems are given in Sec. III. Finally, conclusions are drawn in Sec. IV.

II. MOLECULAR DYNAMICS SETUP

A. Molecular model, force field, and system configuration

The molecular models and system configuration are shown in Fig. 1. In addition to the molecular models of H₂, CO₂, CH₄, and H₂O, as shown in Fig. 1(a), two silica models, i.e., Q2 (9.4 silanol groups/nm²) and Q4 (no silanol group) developed by Heinz *et al.*³⁷ are used to represent the solid-phase component of two typical geological formations. A force field is needed to describe the atom interaction as a function of the position. The potential energy in this study includes the nonbonded and intramolecular energies of the bond stretch and angle bend. The dihedral and improper energies are not considered for silica.³⁸ The potential energy is expressed as

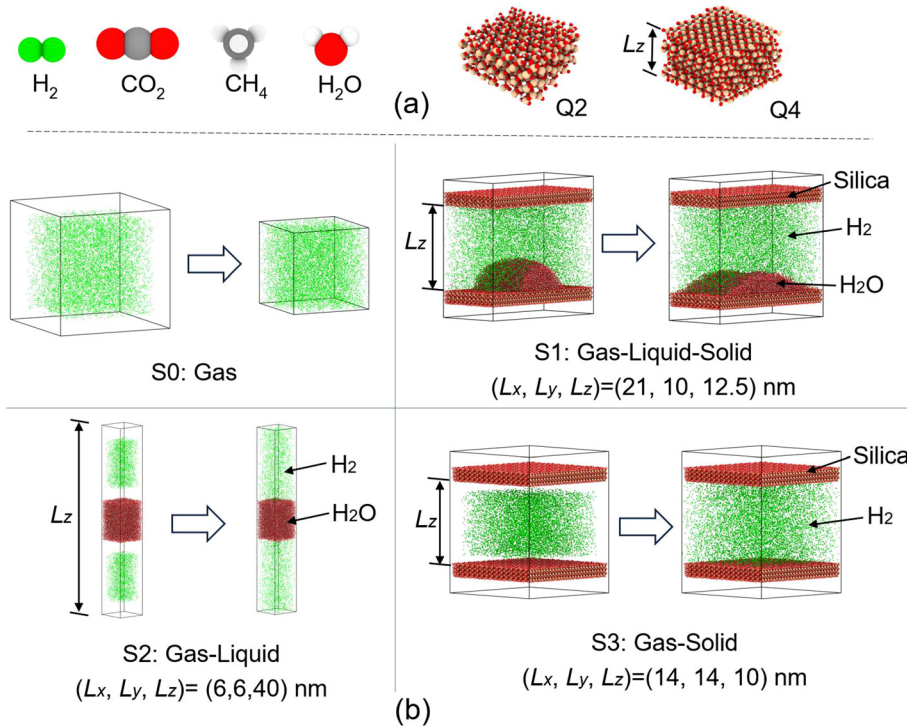


FIG. 1. (a) Molecular models of gases (H₂, CO₂, and CH₄), H₂O, and the silica unit cells (Q2 and Q4). The size of the Q2 and Q4 unit cells in *x*, *y*, and *z* is (34.7, 34.3, 17.8) Å and (33.4, 34.8, 23.9) Å, respectively; (b) initial configurations and equilibrated H₂ systems at 320 K and 20 MPa after 4 ns simulation: *L_x* and *L_y* are the box edge lengths in *x* and *y* directions, respectively; *L_z* of S1 and S3 is the width of the silica nano-slit. The thickness of the H₂O film in S2 is 8.4 nm.

$$E = \frac{q_i q_j}{4\pi\epsilon_0 r_{ij}} + 4\epsilon_{ij} \left[\left(\frac{\sigma_{ij}}{r_{ij}} \right)^{12} - \left(\frac{\sigma_{ij}}{r_{ij}} \right)^6 \right] + k_r (r - r_0)^2 + k_\theta (\theta - \theta_0)^2, \quad (2)$$

where ϵ_0 is the dielectric permittivity of vacuum. q_i and q_j are the charge of particle i and j , respectively. r_{ij} is the distance between particle i and j . ϵ and σ are the energy and size parameters for Lennard-Jones (LJ) potential, respectively. k_r and k_θ are the energy constants. r is the bond length. r_0 is the equilibrium bond length. θ is the angle between two bonds. θ_0 is the equilibrium angle. The interaction between unlike particles is modeled by the Lorentz-Berthelot combining rules: $\sigma_{ij} = (\sigma_{ii} + \sigma_{jj})/2$ and $\epsilon_{ij} = (\epsilon_{ii}\epsilon_{jj})^{1/2}$.

The Interface Force Field (IFF) developed by Wang *et al.*³⁹ and Heinz *et al.*³⁷ is used for H₂ and silica; TraPPE (Transferable Potentials for Phase Equilibria Force Field) for CO₂;⁴⁰ OPLS-AA (Optimized Potentials for Liquid Simulations-All Atoms) for CH₄;⁴¹ and TIP4P for H₂O molecules.⁴² The LJ parameters and charge of the components are listed in Table II. These force fields, i.e., IFF, TIP4P, TraPPE, and OPLS-AA, are compatible with each other and have been used in studying interfacial interactions in multiphase systems under reservoir conditions.^{23,24,43–45} The validation of the force fields and comparison of our results with literature data will be presented in the following.

As shown in Fig. 1(b), a bulk gas system (S0) packed with 10 000 molecules is used to predict transport properties of gases. Three other multiphase systems are also built for studying the aforementioned interfacial properties of the contact angle in system 1 (S1, gas-liquid-solid), the interfacial tension in system 2 (S2, gas-liquid), and gas diffusion under nanoconfinement in system 3 (S3, gas-solid). There are 10 000 water molecules packed in S1 and S2. The silica slabs in S1 and S2 are generated by patterning the unit cell in x and y directions. Different numbers of gas molecules are packed into the box

TABLE II. LJ parameters and charge q of silica, H₂, CO₂, CH₄, and H₂O. M is the additional virtual particle of the TIP4P H₂O model.

	Atom	ϵ_{ii} (kcal/mol)	σ_{ii} (Å)	q (e)
Q2 ³⁷	Si	0.0930	3.6972	+1.1
	O (bulk)	0.0540	3.0914	-0.55
	O (silanol)	0.1220	3.0914	-0.675
Q4 ³⁷	H	0.0150	0.9667	+0.4
	Si	0.0930	3.6972	+1.1
H ₂ ³⁹	O	0.0540	3.0914	-0.55
	H	0.0153	2.9180	0
CO ₂ ⁴⁰	C	0.0536	2.8000	+0.7
	O	0.1569	3.0500	-0.35
CH ₄ ⁴¹	C	0.0660	3.5000	-0.24
	H	0.0300	2.5000	+0.06
H ₂ O ⁴²	O	0.1852	3.1589	0.0000
	H	0	0	0.5564
	M	0	0	-1.1128

accordingly to maintain the pressures in S1, S2, and S3 at the designated values, as shown in Fig. 1. The gas molecular number in Fig. 1 is determined according to the volume occupied by the gas and the number density at the corresponding pressure (Table III).

B. Simulation details

Large-scale Atomic/Molecular Massively Parallel Simulator (LAMMPS) is used for all simulations,⁴⁶ and visualization is performed

TABLE III. Number of gas molecules in multiphase systems.

P (MPa)								
	5	10	20	30	40	50	60	
H ₂	S1	2592	5 043	9 550	13 588	17 222	20 510	23 504
	S2	1236	2 406	4 556	6 482	8 214	9 782	11 210
	S3	2157	4 197	7 949	11 309	14 333	17 070	19 256
CO ₂	S1	3455	14 446	25 855	28 454	30 087	31 308	32 292
	S2	1648	6 890	12 332	13 572	14 350	14 932	15 402
	S3	2876	12 023	21 518	23 682	25 041	26 057	26 876
CH ₄	S1	2840	5 978	12 222	16 969	20 231	22 588	24 404
	S2	1356	2 852	5 830	8 094	9 650	10 774	11 640
	S3	2364	4 976	10 172	14 123	16 838	18 799	20 311

in OVITO (the Open Visualization Tool).⁴⁷ The initial systems are built by PACKMOL.⁴⁸ For S0 and S2, periodical boundary conditions are implemented in all directions. For S1 and S3 with solid silica slabs, periodical boundary conditions are implemented in *x* and *y* directions, while the nonperiodic fixed *ppf* boundary condition is used in the *z* direction. With *ppf*, a vacuum space, the length of which is three times the *z*-edge length, is virtually inserted in the *z* direction to avoid the artifacts generated by the interactions between the real and replicated systems.^{49,50} The cutoff distance for intermolecular interaction is 1.6 nm in real space. The particle–particle particle–mesh (PPPM) algorithm is used for long-range electrostatic interactions in the reciprocal *k*-space with an accuracy of 1×10^{-5} .

All simulations are performed with a time step of 1 fs for two consecutive processes, i.e., equilibrium run for the system to reach stable conditions and production run for collecting data, as shown in Fig. 1(b). In S0, an isothermal-isobaric ensemble (NPT, where N is the number of molecules, P is the pressure, and T is the temperature) is used to maintain the temperature and pressure during the equilibrium run, followed by a canonical ensemble (NVT, where V is the volume) in the production run to maintain a constant volume and the temperature. In NPT and NVT simulations, the damping factors for the Nosé–Hoover thermostat and barostat are 100 and 1000 times of the

time step, respectively. For multiphase systems, the Berendsen thermostat is used to maintain the temperature with a damping factor of 100. For S1 and S3, a 5 Å layer of the outmost silica molecules is kept fixed.

III. RESULTS

A. Density and viscosity of bulk-gas S0 system

As shown in Fig. 2, the densities and viscosities obtained from bulk MD simulations are compared with the data from NIST Chemistry Webbook.²² The converging process of the viscosity is shown in Fig. 2(a), and the final values of the density and viscosity are shown in Figs. 2(b) and 2(c), respectively. Viscosity is calculated using the Green–Kubo method^{51,52} in NVT ensemble by

$$\eta = \frac{V}{3k_B T} \int_0^\infty \langle \langle P_{\alpha\beta}(0)P_{\alpha\beta}(t) \rangle \rangle dt, \tag{3}$$

where *V* is the volume, *k_B* is the Boltzmann constant, *T* is the temperature, *P_{αβ}* represents the *αβ* components of the pressure tensor, *α* and *β* are any two of the *x*, *y*, or *z* Cartesian coordinates, and $\langle \dots \rangle$ indicates ensemble average. According to the work of Nie *et al.*,⁵³ the correlation length is set to be 10 ps with a sampling interval of 1 fs for pressure tensor. The final value of the viscosity in Fig. 2(c) is the averaged results of the last 2 ns data of Fig. 2(a).

In Figs. 2(b) and 2(c), both the density and viscosity of the gases agree well with the NIST data, indicating that the equilibrium molecular dynamics (EMD) simulation can be employed to predict the transport properties of binary/ternary mixtures over a wide range of reservoir conditions. H₂ densities are underestimated slightly, and the maximum absolute relative deviation for H₂, CO₂, and CH₄ is 5.1%, 2.4%, and 4.2%, respectively. H₂ and CH₄ densities increase gradually with pressure passing across the critical pressure, whereas there is a dramatic change for CO₂ from 5 to 20 MPa. The extremely low density of H₂ makes it difficult to displace H₂O in under-surface porous media. The substantial density difference between H₂ and CO₂/CH₄ indicates that a strong gravity override and density segregation will occur during UHS operation, resulting in great upward movement of H₂ toward the caprock than CH₄ and CO₂. Regarding the viscosity, the maximum deviation for H₂ occurs at 5 MPa, which is 5.3% lower

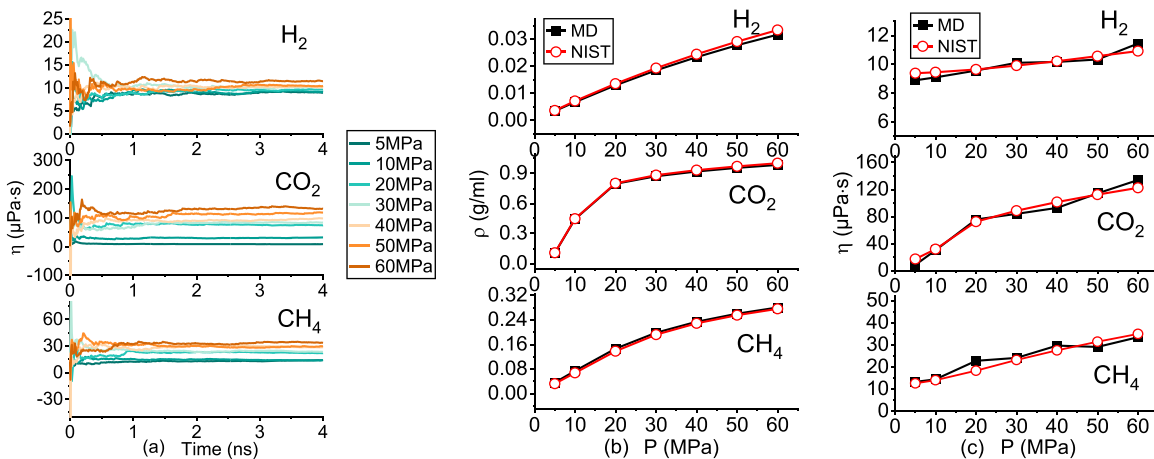


FIG. 2. (a) Convergence of gas viscosity using GK method; (b) effects of pressure on density; and (c) effects of pressure on viscosity.

than NIST data, and the averaged absolute deviation of CO₂ and CH₄ viscosities are 12.1% and 8.0%, respectively. Compared with CO₂ and CH₄, the H₂ viscosity is only slightly influenced by pressure. A low viscosity of H₂ can facilitate its injection and extraction, but it can also result in undesired viscous fingering.^{5,54}

B. Wettability of gas-water-silica S1 system

Wetting mechanics is the synergistic effects between the interactions of gas-water, gas-solid, and water-solid phases. The effects of the gas temperature and pressure on wettability can be quantified by the alternation of the water contact angle. The droplet morphology and the contact angles are demonstrated in Fig. 3. First, the time evolution of the center of mass (COM) of the water droplet on Q2 silica in the z direction is evaluated in Fig. 3(a). The decrease in the COM-z of the droplet is because the silanol groups on Q2 surface can form the hydrogen bonding with water, which leads to the gradually spreading of water molecules over the silica surface. The water droplet spread much more slowly when enveloped by CO₂ than by CH₄, while H₂ can hardly alter the spreading process. CO₂ has high affinity with silica because of the strong electrostatic interaction as CO₂ has quadrupole polarizability. There is only vdW intermolecular interactions between

H₂ and silica. The morphology of the water droplet is stable as the COM would not change with time after 4 ns, and the snapshots of the systems at 20 MPa are shown in Fig. 3(b). The water droplet on Q2 is flattened, while the droplet can almost be detached from the Q4 surface when enveloped by CO₂.

As shown in Fig. 3(c), the contact angle is computed by the 2D density profile of the water droplet, which is averaged over 4–6 ns using bins of 0.5 × 0.5 Å. A circular profile is fitted at the gas-liquid interface where the iso-density is in the range of 0.2–0.4 g/ml.^{26,55} The contact angle is determined by

$$(x - a)^2 + (z - b)^2 = R^2, \tag{4}$$

$$\theta = \arccos\left(\frac{z_0 - b}{R}\right), \tag{5}$$

where *a* and *b* are the coordinates of the center of the fitted circle in *x* and *z* directions, respectively. *R* is the radius. *z*₀ is the height of the contact plane, which is the average position of the outmost silica atoms,^{23,56} i.e., 19.3 for Q2 and 26.5 Å for Q4.

The contact angles of H₂/CO₂/CH₄-H₂O-silica systems are summarized in Fig. 4. For comparison, representative experimental data of a gas-water/brine-quartz system are collected and plotted. The tilted

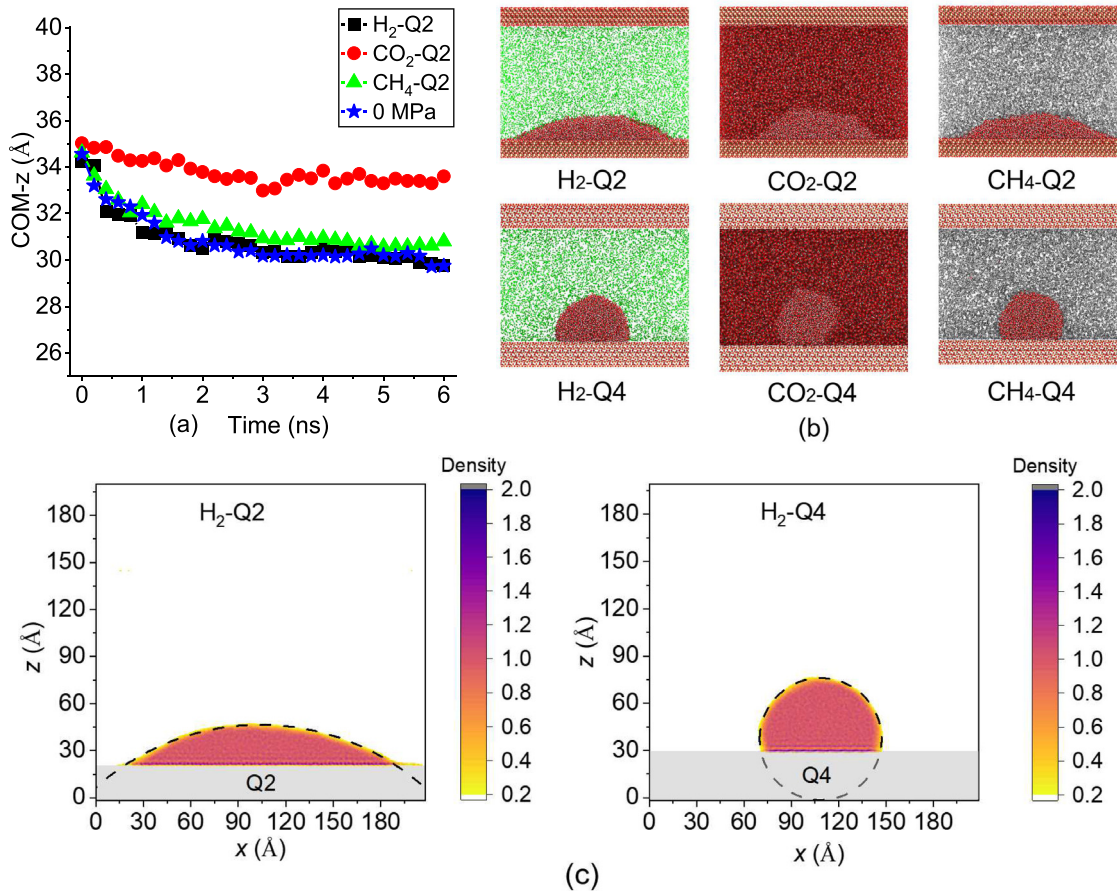


FIG. 3. (a) Time evolution of H₂O droplet COM-z at 20 MPa; (b) system snapshots at 20 MPa after 6 ns; and (c) density contour plots of H₂O droplet in H₂-H₂O-silica S1 systems. The black dashed lines show the fitted circles.

01 February 2024 13:23:46

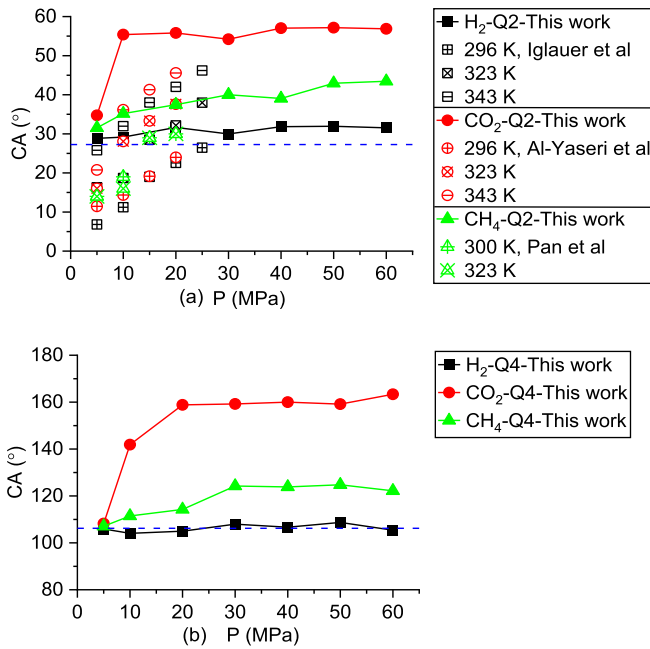


FIG. 4. Effects of gas pressure on contact angle of water: (a) gas-H₂O-Q2 system and (b) gas-H₂O-Q4 system. The dashed lines are the contact angles of water at 0 MPa. Reference experimental data: H₂-brine (10 wt. % NaCl)-quartz: Reproduced with permission from Iglaue *et al.*, *Geophys. Res. Lett.* **48**, e2020GL090814 (2021). Copyright 2021 John Wiley and Sons.⁵⁷ CO₂-deionized water-quartz: Reproduced with permission from Al-Yaseri *et al.*, *J. Chem. Thermodyn.* **93**, 416 (2016). Copyright 2016 Elsevier.⁵⁸ CH₄-brine (1.5 wt. % NaCl)-quartz: Reproduced with permission from Pan *et al.*, *Energy Fuels* **33**, 788 (2019). Copyright 2019 American Chemical Society.⁵⁹ All experimental CA values at 0 MPa are zero.^{57–59}

plate technique was used in experiments, and two contact angles were generated, i.e., advancing contact angle (θ_a) and receding contact angle (θ_r). The equilibrium contact angle (θ_e) can be obtained by¹¹

$$\theta_e = \arccos\left(\frac{N_a \cos \theta_a + N_r \cos \theta_r}{N_a + N_r}\right), \quad (6)$$

$$N_a = \left(\frac{\sin^3 \theta_a}{2 - 3\cos \theta_a + \cos^3 \theta_a}\right)^{\frac{1}{3}}, \quad (7)$$

$$N_r = \left(\frac{\sin^3 \theta_r}{2 - 3\cos \theta_r + \cos^3 \theta_r}\right)^{\frac{1}{3}}. \quad (8)$$

The contact angle of water without an ambient gas (i.e., 0 MPa) on Q2 silica at 320 K is 27.3°, which indicates the silica is strongly hydrophilic, whereas the water contact angle on Q4 silica is 106.2°, indicating the silica is strongly hydrophobic. At the interface, a CA smaller than 90° corresponds to high wettability or hydrophilicity, whereas a contact angle larger than 90° signifies low wettability or hydrophobicity. The results are consistent with the earlier reported MD simulation results of 103.8° for a H₂O (SPC/Fw model)-Q4 system at 300 K.⁵⁰ The contact angle in the CO₂-H₂O-Q4 system is 141.9° at 10 MPa, which is close to 146.7° at 10.5 MPa and 318 K reported by Chen *et al.*,²³ who used the flexible SPC water and EPM2 CO₂ models.

In Fig. 4, CA follows the order of $\theta^{\text{CO}_2} > \theta^{\text{CH}_4} > \theta^{\text{H}_2}$ in both experiments and MD simulations under the same thermodynamic condition and with the same silica substrate. This implies that CO₂ has higher wettability and, therefore, is more favorable than CH₄ as the cushion gas for withdrawing H₂. At 323 K, the measured CA is increased by 16°, 21°, and 16° for H₂, CO₂, and CH₄, respectively, when the pressure is increased from 5 to 20 MPa. The experimental results also reveal that CA increases with the temperature for CO₂/H₂-water/brine-quartz systems, but not for CH₄ where the CA has the same value at 300 and 320 K. The effects of the temperature on wettability depend on minerals, and the mechanism is not yet fully understood.^{20,60,61} Moreover, different measurement procedures and sample cleaning processes in experiments could result in the uncertainties of CA and the inconsistency of its temperature dependence.²⁴ It has been widely accepted that CA increases with the CO₂ pressure for various minerals, which is attributed to an increased gas molecular density and enhanced intermolecular interaction between the gas and rock surface.^{60,62,63}

As for H₂, a linear correlation between $\cos \theta$ and gas density (ρ) is well fitted for H₂-H₂O-mica/clay/basalt systems, with R^2 (goodness of fit) higher than 90% at 330 K and 0–20 MPa.¹¹ However, it should be mentioned that some experiments found that CA is not affected by the temperature and pressure in H₂/CH₄-water/brine-sandstone systems when the captive bubble method was used.^{64,65} In MD simulations using a sessile water droplet, CA is increased by 21° and 50° when the CO₂ pressure is increased to 10 and 20 MPa in Q2 and Q4 silica systems, respectively. The CA is only increased by 4° and 7° in Q2 and Q4 silica systems, respectively, when the CH₄ pressure is increased to 30 MPa, which is much less noticeable than in experiments. Effects of the H₂ pressure on CA show a different trend between MD and experimental data, and there is almost no change to CA in the MD simulations for both Q2 and Q4 silica in conditions up to 60 MPa. It can be seen from Fig. 4 that for hydrophobic Q4 silica, H₂ virtually does not change the contact angle of water at 0 MPa, i.e., under no impact of any gas components, even when the pressure is increased to 60 MPa. For hydrophilic Q2 silica, H₂ tends to increase the water contact angle in vacuum, but only slightly compared to CH₄ and CO₂. The slight increase is also independent of the pressure, similar to what is observed for Q4 silica. Due to a much weaker intermolecular interaction with the rock surface together with a low molecular mass and thus volume, H₂'s capability of adsorbing on to either the Q2 or Q4 silica surface is low, even in supercritical fluid state as the system pressure far exceeds its critical one (the system temperature is much higher than the critical one of all the three gases). According to Ref. 60, $\cos \theta + 1 \propto \gamma_{G,H_2O}^{-1}$, i.e., the contact angle is largely determined by the surface tension force between water and the gas in such a system. As shown in Fig. 5(c), the H₂/H₂O surface tension is independent of pressure, which is also corroborated by experimental data shown in the figure. Therefore, the effects of H₂ on wettability is low, and the water contact angle is independent of the H₂ pressure, either with a hydrophilic or hydrophobic silica substrate. Moreover, although considerable discrepancy or inconsistency of experimental CA data for CO₂-water/brine-rock/shale^{16,18,66} and H₂-water/brine-rock systems have been seen, our MD results are consistent with literatures.^{67,68}

The CA at above 30 MPa is almost constant for all gases in MD simulation, and a further increase in the pressure has negligible effects on wettability. At $P > 30$ MPa, the adsorbed CH₄ and CO₂ on the silica surface would not change notably with the pressure, indicated by the

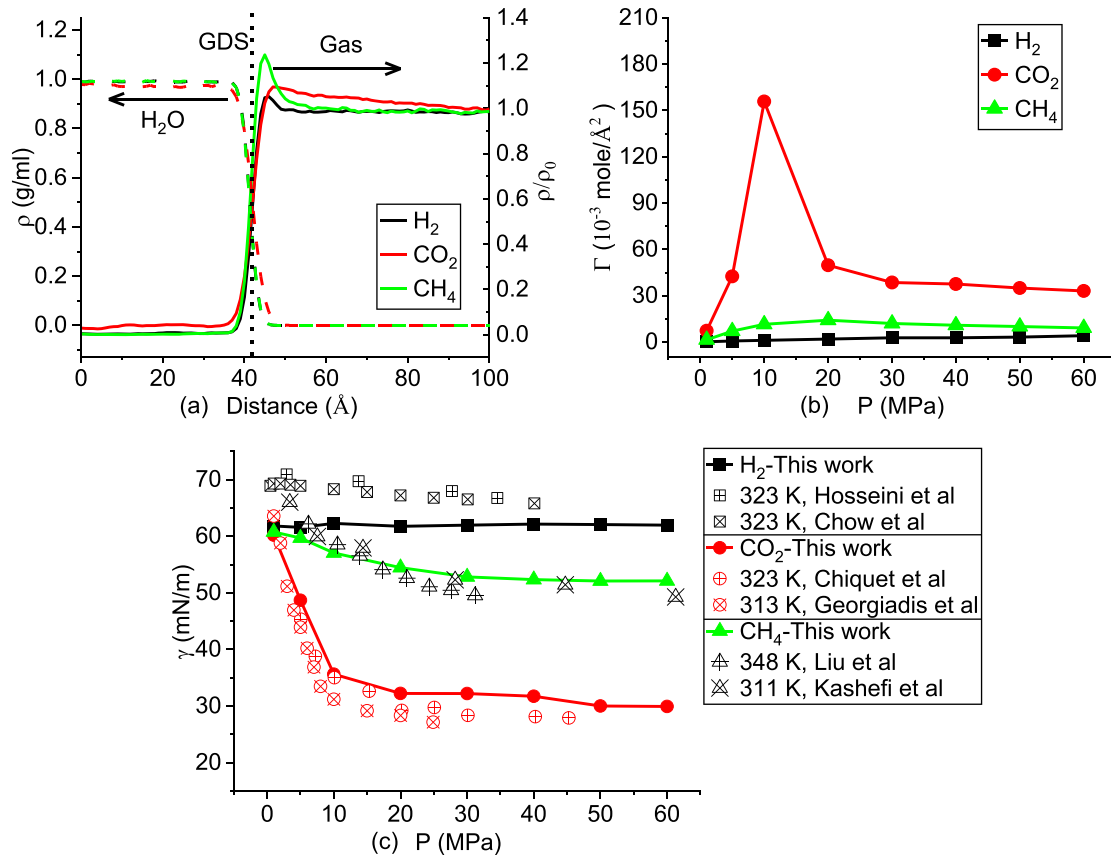


FIG. 5. (a) Density profiles of water and reduced density profiles (ρ/ρ^{bulk}) of gases at 20 MPa, where the black dotted line indicates the GDS of H₂-H₂O located at $z = 41.84\text{\AA}$; (b) effects of pressure on surface excess adsorption at 1 MPa and 5–60 MPa; and (c) effects of pressure on IFT. Reference experimental data: Reproduced with permission from Hosseini *et al.*, *J. Pet. Sci. Eng.* **213**, 110441 (2022). Copyright 2022 Elsevier.⁷³ Reproduced with permission from Chow *et al.*, *Fluid Phase Equilib.* **475**, 37 (2018). Copyright 2018 Elsevier.⁷⁴ Reproduced with permission from Chiquet *et al.*, *Energy Convers. Manage.* **48**, 736 (2007). Copyright 2007 Elsevier.⁷⁵ Reproduced with permission from Georgiadis *et al.*, *J. Chem. Eng. Data* **55**, 4168 (2010). Copyright 2010 American Chemical Society.⁷⁶ Reproduced with permission from Liu *et al.*, *Ind. Eng. Chem. Res.* **55**, 12358 (2016). Copyright 2016 American Chemical Society.⁷⁷ Reproduced with permission from Kashefi *et al.*, *Fluid Phase Equilib.* **409**, 301 (2016). Copyright 2016 Elsevier.⁷⁸

peak densities shown in Fig. 6. In addition, the contact angle is largely determined by and inversely proportional to the surface tension force between water and the gas in such a system, as stated above. As shown in Fig. 5(c), the surface tension of the three gases, both experimental and MD data, shows little dependence on the pressure. Therefore, the CA has little dependence on pressures higher than 30 MPa.

For CGS applications, most previous MD modeling studies of CO₂-water/brine-rock systems is at pressures below 25 MPa.^{23,24,26,54,55,69,70} In a recent study by Zhou *et al.*,⁴⁹ it is found that contact angles keep increasing gradually with a reduced growth rate in a CO₂-H₂O-kerogen system, changing from strongly H₂O-wet (CA = 60.4° at 0 MPa) to strongly CO₂-wet (CA = 180° at 44 MPa), which implies that the effects of a higher pressure on H₂ wettability over an organic substrate should be investigated, considering coal seams are also a feasible reservoir type for UHS.^{11,71}

C. Interfacial properties of gas-water S2 system

The interfacial properties of the gas-water system S2 are evaluated by the gas/water density, surface excess (Γ) and IFT (γ), as

demonstrated in Fig. 5. The Gibbs dividing surface (GDS) is used to identify the position of the interface where the surface excess of water is zero from the density profile of water,^{30,72} as shown in Fig. 5(a). The gases have a positive surface activity and can accumulate at the gas-water interface, where the gas density is higher than that away from the interfacial region. The positions of the peak values of CH₄ and H₂ are closer to GDS than CO₂.

The surface excess of gas i relative to water (Γ_i^w) is used to quantify the gas adsorption tendency to water at the interface, expressed as^{30,72}

$$\Gamma_i^w = \frac{N_i^{\text{total}} - C_i^I V_I - C_i^{\text{II}} V_{\text{II}}}{A}, \quad (9)$$

where N is the total number of gas molecules, C is the number density of the gas, I and II denote, respectively, the gas- and water-rich bulk phases distinguished by the GDS, V is the volume of phase I or II, and A is the area of interfaces.

The surface tension is computed by^{30,72}

$$\gamma = \frac{L_z}{2} \left[P_{zz} - \frac{1}{2} (P_{xx} + P_{yy}) \right], \quad (10)$$

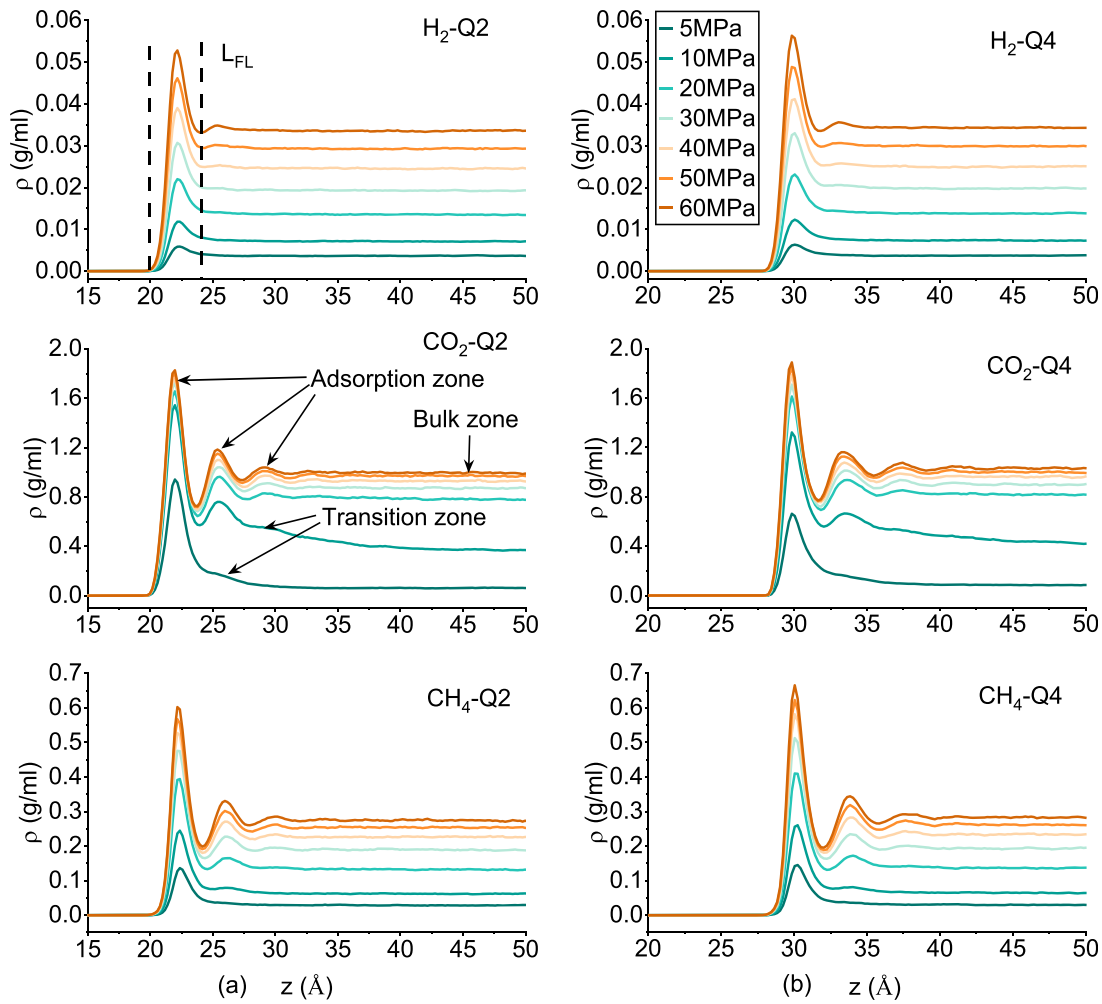


FIG. 6. Gas density profile along the direction normal to the silica surface at different pressures: (a) gas confined by Q2 silica and (b) gas confined by Q4 silica. The dashed lines indicate the thickness of the first adsorption layer.

where P_{xx} is a diagonal component of the pressure tensor, and the pre-factor of $1/2$ considers the existence of two interfaces in the simulation box.

The surface excess follows the order of $\Gamma_{\text{CO}_2}^w > \Gamma_{\text{CH}_4}^w > \Gamma_{\text{H}_2}^w$ under all conditions, as shown in Fig. 5(b). $\Gamma_{\text{CO}_2}^w$ increases rapidly to the peak value of $0.156 \text{ mol}/\text{\AA}^2$ at 10 MPa, then drops to $0.05 \text{ mol}/\text{\AA}^2$ at 20 MPa, followed by a slow decrease with the pressure. $\Gamma_{\text{CH}_4}^w$ increases gradually with the pressure to the peak value at 20 MPa and then decreases. $\Gamma_{\text{H}_2}^w$, on the other hand, increases monotonously with the pressure. The IFT results of MD simulation agree well experimental data for both CO_2 and CH_4 , as shown in Fig. 5(c). The H_2 -water IFT is underestimated by $\sim 11\%$ on average as compared to the experimental values. Contrary to the surface excess, IFT follows the order of $\gamma^{\text{CO}_2} < \gamma^{\text{CH}_4} < \gamma^{\text{H}_2}$ under all conditions. The CH_4 -water IFT decreases gradually with the pressure with a reduced rate. There is a clear turning point for CO_2 -water IFT at ~ 10 MPa where the IFT decreases remarkably by 42%, followed by a slight decrease with the pressure. In the experiment, the H_2 -water IFT decreases slightly with

the pressure at a reduction rate of $-0.01 \text{ mN}\cdot\text{m}^{-1}/\text{MPa}$ on average for temperatures ranging from 298 to 423 K,⁷³ while there is no pressure dependence observed in MD simulation at 320 K. H_2 can hardly alter the IFT because the IFT-pressure correlation is associated with the density difference between the gas and water.¹¹ Moreover, the intermolecular vdW interaction contributes scarcely to the gas-water interaction at GDS from the energy decomposition perspective.⁷⁹

D. Nanoconfined adsorption and diffusion behavior of gas-silica S3 system

The gas adsorption in nano-slits can be characterized by the gas density profile, as demonstrated in Fig. 6. The simulation time is 2 ns for all cases. The density profile is computed by

$$\rho(z) = \frac{M_{\text{gas}} \langle N_i(z + \Delta z) \rangle}{L_x L_y \Delta z}, \quad (11)$$

where Δz is the bin size 0.2 \AA , M is the molecule weight, and N is the number of gas molecules in the bin.

The gas density varies with the distance away from the outmost atoms of the silica substrate. The silica nano-slit can be divided into three regions according to the density profile, i.e., adsorption zone, transition zone, and bulk zone.^{80,81} Gas molecules accumulate in the region close to the silica surface forming adsorption layers, featuring peak values in the density profile. The density in the adsorption zone decreases further away from the silica surface owing to a diminishing gas-silica interaction. Further away from the transition zone and approaching the slit center, the bulk-fluid region would be formed where surface effects are negligible, molecules can move freely, and the density does not change with position anymore. The transition zone of CO₂ at 5 and 10 MPa is 0.5–1.0 nm, which is wider than that of CH₄ and H₂, both less than 0.3 nm. The thickness of the first adsorption layer (L_{FL}) of H₂ in both Q2 and Q4 systems is 0.4 nm, which is consistent with the theoretical prediction 0.3–0.5 nm.^{80,81}

The density profile depends strongly on the pressure and gas type, but only slightly on the silica type of Q2/Q4. For H₂ in both Q2 and Q4 systems, there is only one adsorption layer at pressures below 50 MPa. The second layer can be discerned at 60 MPa, which is only 1.03 times denser than in the bulk region. The second adsorption layers are formed clearly at pressures above 10 and 20 MPa for CO₂

and CH₄, respectively, in both Q2 and Q4 systems. There is even a third adsorption layer of CO₂ and CH₄, which can be seen at pressures above 30 and 50 MPa, respectively. The density of H₂ in the adsorption zone increases linearly with the pressure in both Q2 and Q4 systems, with R^2 of the linear fitting equal to 99.1% and 98.6%, respectively. The peak values of the first adsorption density in Q2 is 1.44 times higher than that of the bulk density obtained from the linear fitting of $\rho^{peak} \sim \rho^{bulk}$, and 1.32 for H₂-Q4 system. For CH₄ and CO₂ in both Q2 and Q4 systems, the density increases with a declined growth rate for both the first and second adsorption layers.

The effects of nanoconfinement on mobility properties of the gases are compared by the mean square displacement (MSD) and diffusion coefficient (D), as shown in Figs. 7 and 8, respectively. MSD is a measure of the deviation of the particle position with respect to its initial position over time, expressed as

$$\langle r^2(t) \rangle = \frac{1}{N} \left\langle \sum_{i=1}^N |\mathbf{r}^{(i)}(t) - \mathbf{r}^{(i)}(0)|^2 \right\rangle, \quad (12)$$

where N is the number of particles, and vector $\mathbf{r}^{(i)}(t)$ is the position of the i th particle at time t .

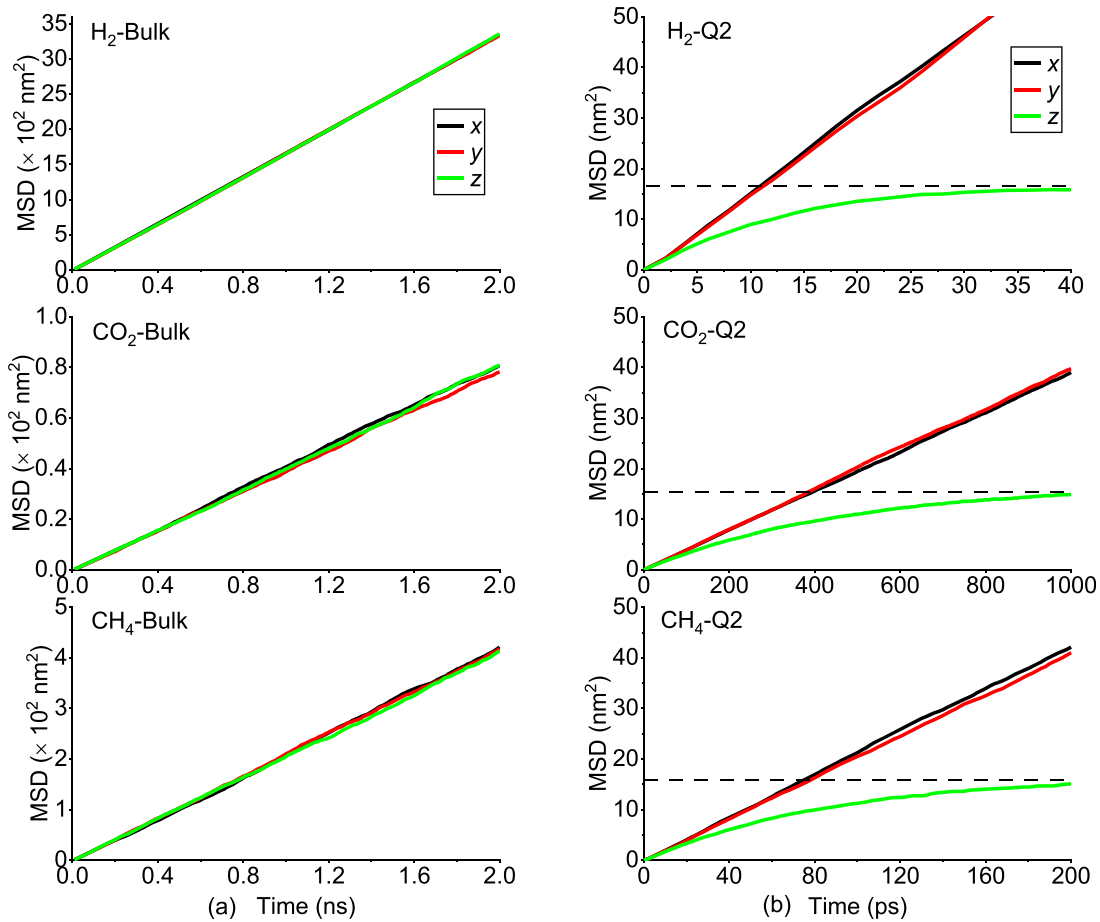


FIG. 7. (a) MSD of gases in x, y, and z directions in the bulk-gas system S0 at 20 MPa and (b) MSD of gases in Q2 nano-slit at 20 MPa. The dashed lines in (b) indicate the boundaries of the plateaus.

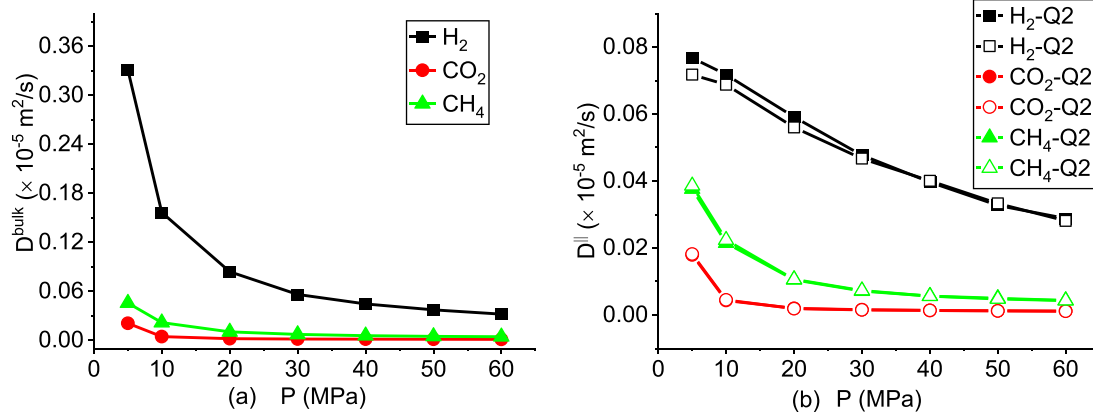


FIG. 8. (a) Effects of pressure on the diffusion coefficients of gases in the bulk system. $D^{\text{bulk}} = (D^x + D^y + D^z)/3$ and (b) effects of pressure on the planar diffusion in the Q2/Q4 silica nano-slit, $D^{\parallel} = (D^x + D^y)/2$.

As shown in Fig. 7(a), MSD's of the gases in x , y , and z directions overlap with each other due to the isotropy intrinsic of the bulk system. MSD correlates linearly with time as gas molecules undergo Brownian motion, featuring normal diffusion.⁸² The diffusion coefficient can be extracted from the slope of the MSD using $\langle r^2(t) \rangle = 2dDt$, where d is the number of dimensions. According to Zhong *et al.*,⁸³ a system of more than 500 gas molecules is large enough to avoid the finite-size effect on self-diffusion.

The MSD of H_2 has a much larger slope than that of CH_4 and CO_2 at 20 MPa. For gases in the nanoconfined system S3, the MSD's in the planar x and y directions also overlap with each other and increase linearly with time. However, in the confined z direction, gas molecules undergo sub-diffusive motion, featuring anomalous diffusion.^{82,84} As shown in Fig. 7(b), the MSD in the z direction increases nonlinearly with a reduced growth rate until it reaches the plateau value at $\sim 15\text{--}17 \text{ nm}^2$, and the H_2 case reaches a plateau much faster than CH_4 and CO_2 . This is consistent with the theoretical value of 16.67 nm^2 , as analyzed by Wang and Hadjiconstantinou⁸⁵ that MSD approaches the value of $L_z^2/6$ after the time is longer than a characteristic time scale. The diffusion in the normal direction would affect the swap frequency of the gases between the adsorption and bulk regions.

The planar motion is the primary reason causing the leakage of gases in underground porous formation.⁶ The effect of space confinement is studied by comparing the difference between the planar diffusion coefficient (D^{\parallel}) in the nanoconfined system and the diffusion coefficient in the bulk system (D^{bulk}), as shown in Fig. 8. The diffusion coefficient follows the order of $D^{\text{H}_2} > D^{\text{CH}_4} > D^{\text{CO}_2}$ in both the bulk and confined systems under all conditions. The diffusion coefficient of a gas decreases with the pressure due to the increased intermolecular friction according to gas-kinetic theory. The D^{bulk} of $\text{H}_2/\text{CO}_2/\text{CH}_4$ decreases drastically from 5 to 20 MPa by a factor of 3.94, 10.43, and 4.36, respectively, followed by gradual decreasing with the pressure. The D^{\parallel} of CO_2 and CH_4 in the confined system has a similar trend to D^{bulk} , while D^{\parallel} of H_2 decreases linearly with the pressure in the confined system. The silica type has negligible effects on planar diffusion of the gases. At 5, 10, and 20 MPa, the confinement effect on H_2 diffusion is evident as the ratios of $D^{\parallel}/D^{\text{bulk}}$ are ~ 0.23 , 0.46, and 0.70, respectively. At higher pressures of 30–60 MPa, the confinement effect

weakens as the ratio ranges in 0.85–0.99 for all gases. It should be mentioned that the pore size also plays a crucial role in gas adsorption and diffusion. For example, the bulk zone would disappear when the slit is narrower than the critical size, e.g., 2 nm for CH_4 in Montmorillonite slit pore at 323 K.⁸⁶

IV. CONCLUSIONS

The reliable data of transport and interfacial physics of $\text{H}_2/\text{CO}_2/\text{CH}_4$ interacting with H_2O and/or rock are essential for understanding H_2 injection, storage, and withdrawal mechanisms, particularly when CO_2 or CH_4 is used as the cushion gas. Molecular dynamics simulation was performed at 320 K to study the effects of H_2 pressure (up to 60 MPa) on transport properties (density, viscosity, and diffusion coefficient) in the bulk system, and interfacial properties (wettability, interfacial tension, surface adsorption, and confined diffusion) in contact with water and/or silica. The H_2 properties in the three systems are compared with those of CO_2 and CH_4 . Two silica molecular models are built, i.e., hydrophilic Q2 and hydrophobic Q4. The conclusions are summarized as follows:

The density and viscosity predicted by equilibrium molecular dynamics agree well with experimental data. The density and viscosity of H_2/CH_4 increase gradually with the pressure, while there is a drastic change for CO_2 as the pressure crosses the critical value.

The contact angles of water on both the Q2 and Q4 silica increase with the gas pressure of CH_4 and CO_2 until reaching a plateau at 10–30 MPa. H_2 has a much lower wettability than CO_2 and can barely alter the water contact angle even at 60 MPa.

Similar to CO_2 and CH_4 , H_2 molecules can also accumulate at the interface with water. The surface excess of H_2 increases monotonically with the pressure, but at a much lower rate than that of CO_2 . Effects of the H_2 pressure on the interfacial tension are negligible, while CH_4 can slightly reduce the IFT. The interfacial tension of CO_2 –water decreases significantly when the pressure is increased to 10 MPa but can remain almost unchanged at pressures above 20 MPa.

Confined by the nano-slit of 10 nm, the first adsorption layer of H_2 has a thickness of 0.4 nm. The second adsorption layer of H_2 , CO_2 , and CH_4 emerges at 50, 10, and 20 MPa, respectively. The density of H_2 in the adsorption zone increases linearly with the pressure. Gas molecules undergo sub-diffusive motion in the confined direction, and

the planar motion is still in the normal diffusion regime. H_2 planar diffusion is slowed down evidently due to the nanoconfinement effects at pressures lower than 20 MPa. Silanol functional groups on the silica surface have insignificant effects on gas diffusion.

These fundamental data and findings can be used as input parameters for predicting the capillary pressure, gas column height, and the IFT of the porous media in the context of UHS. Moreover, the MD systems configured in this study can be extended to predict properties of the binary gas mixtures as there is a mixing zone in UHS between H_2 and the cushion gas.

ACKNOWLEDGMENTS

This work was supported by the Engineering and Physical Sciences Research Council (EPSRC) under Grant No. EP/T033940/1. The authors are grateful to the high-performance computing (HPC) resources of ARCHER2 supported by the EPSRC Access to High Performance Computing under Project No. e774 and UK Materials and Molecular Modelling Hub for computational resources, which is funded by EPSRC (Grant Nos. EP/T022213/1, EP/W032260/1, and EP/P020194/1).

AUTHOR DECLARATIONS

Conflict of Interest

The authors have no conflicts to disclose.

Author Contributions

Cheng Chen: Conceptualization (lead); Data curation (lead); Formal analysis (lead); Investigation (lead); Methodology (lead); Resources (lead); Software (lead); Validation (lead); Visualization (lead); Writing – original draft (lead). **Jun Xia:** Conceptualization (supporting); Funding acquisition (lead); Investigation (supporting); Project administration (lead); Resources (supporting); Supervision (lead); Writing – review & editing (lead).

DATA AVAILABILITY

The data that support the findings of this study are openly available in figshare at https://figshare.com/articles/dataset/cc_gas-liquid-solid/24438541, Ref. 87.

REFERENCES

- J. O. Abe, A. Popoola, E. Ajenifuja, and O. M. Popoola, "Hydrogen energy, economy and storage: Review and recommendation," *Int. J. Hydrogen Energy* **44**, 15072–15086 (2019).
- S. S. Kumar and H. Lim, "An overview of water electrolysis technologies for green hydrogen production," *Energy Rep.* **8**, 13793–13813 (2022).
- IEA, *Global Hydrogen Review* (IEA, Paris, 2022).
- N. Heinemann, J. Alcalde, J. M. Miocic, S. J. Hangx, J. Kallmeyer, C. Ostertag-Henning, A. Hassanpouryouzband, E. M. Thaysen, G. J. Strobel, and C. Schmidt-Hattenberger, "Enabling large-scale hydrogen storage in porous media – The scientific challenges," *Energy Environ. Sci.* **14**, 853–864 (2021).
- A. Aftab, A. Hassanpouryouzband, Q. Xie, L. L. Machuca, and M. Sarmadivaleh, "Toward a fundamental understanding of geological hydrogen storage," *Ind. Eng. Chem. Res.* **61**, 3233–3253 (2022).
- N. S. Muhammed, B. Haq, D. Al Shehri, A. Al-Ahmed, M. M. Rahman, and E. Zaman, "A review on underground hydrogen storage: Insight into geological sites, influencing factors and future outlook," *Energy Rep.* **8**, 461–499 (2022).
- N. S. Muhammed, B. Haq, and D. Al Shehri, "CO₂ rich cushion gas for hydrogen storage in depleted gas reservoirs: Insight on contact angle and surface tension," *Int. J. Hydrogen Energy* **50**, 1281 (2023).
- N. S. Muhammed, B. Haq, and D. Al Shehri, "Role of methane as a cushion gas for hydrogen storage in depleted gas reservoirs," *Int. J. Hydrogen Energy* **48**, 29663 (2023).
- B. Pan, X. Yin, Y. Ju, and S. Iglauer, "Underground hydrogen storage: Influencing parameters and future outlook," *Adv. Colloid Interface Sci.* **294**, 102473 (2021).
- B. Pan, K. Liu, B. Ren, M. Zhang, Y. Ju, J. Gu, X. Zhang, C. R. Clarkson, K. Edlmann, and W. Zhu, "Impacts of relative permeability hysteresis, wettability, and injection/withdrawal schemes on underground hydrogen storage in saline aquifers," *Fuel* **333**, 126516 (2023).
- M. Aslannezhad, M. Ali, A. Kalantariasl, M. Sayyafzadeh, Z. You, S. Iglauer, and A. Keshavarz, "A review of hydrogen/rock/brine interaction: Implications for hydrogen geo-storage," *Prog. Energy Combust. Sci.* **95**, 101066 (2023).
- H. Shi, Q. Zhu, Z. Chen, J. Li, D. Feng, S. Zhang, J. Ye, and K. Wu, "Pore-scale modeling of water-gas flow in heterogeneous porous media," *Phys. Fluids* **35**, 072114 (2023).
- S. Zhang, J. Li, Z. Chen, K. Wu, and Q. Zhu, "Investigation on spontaneous liquid-liquid imbibition in capillaries with varying axial geometries using lattice Boltzmann method," *Phys. Fluids* **35**, 122108 (2023).
- X. Guo, H. Yan, and H. Liu, "New insights into the Haines jump in immiscible two-phase flow displacement," *Phys. Fluids* **35**, 013311 (2023).
- S. Iglauer, C. Pentland, and A. Busch, "CO₂ wettability of seal and reservoir rocks and the implications for carbon geo-sequestration," *Water Resour. Res.* **51**, 729–774, <https://doi.org/10.1002/2014WR015553> (2015).
- M. Arif, S. A. Abu-Khamsin, and S. Iglauer, "Wettability of rock/CO₂/brine and rock/oil/CO₂-enriched-brine systems: Critical parametric analysis and future outlook," *Adv. Colloid Interface Sci.* **268**, 91–113 (2019).
- M. Arif, Y. Zhang, and S. Iglauer, "Shale wettability: Data sets, challenges, and outlook," *Energy Fuels* **35**, 2965–2980 (2021).
- B. Pan, X. Yin, and S. Iglauer, "A review on clay wettability: From experimental investigations to molecular dynamics simulations," *Adv. Colloid Interface Sci.* **285**, 102266 (2020).
- B. Pan, T. Ni, W. Zhu, Y. Yang, Y. Ju, L. Zhang, S. Chen, J. Gu, Y. Li, and S. Iglauer, "Mini review on wettability in the methane-liquid-rock system at reservoir conditions: Implications for gas recovery and geo-storage," *Energy Fuels* **36**, 4268–4275 (2022).
- M. Sarmadivaleh, A. Z. Al-Yaseri, and S. Iglauer, "Influence of temperature and pressure on quartz-water-CO₂ contact angle and CO₂-water interfacial tension," *J. Colloid Interface Sci.* **441**, 59–64 (2015).
- H. Yu, H. Xu, J. Fan, Y.-B. Zhu, F. Wang, and H. Wu, "Transport of shale gas in microporous/nanoporous media: Molecular to pore-scale simulations," *Energy Fuels* **35**, 911–943 (2020).
- E. W. Lemmon, M. L. Huber, and M. O. McLinden, "NIST reference fluid thermodynamic and transport properties – REFPROP," NIST Standard Reference Database Report No. 23 (2002).
- C. Chen, N. Zhang, W. Li, and Y. Song, "Water contact angle dependence with hydroxyl functional groups on silica surfaces under CO₂ sequestration conditions," *Environ. Sci. Technol.* **49**, 14680–14687 (2015).
- C. Chen, B. Dong, N. Zhang, W. Li, and Y. Song, "Pressure and temperature dependence of contact angles for CO₂/water/silica systems predicted by molecular dynamics simulations," *Energy Fuels* **30**, 5027–5034 (2016).
- C. Chen, Z. Chai, W. Shen, and W. Li, "Effects of impurities on CO₂ sequestration in saline aquifers: Perspective of interfacial tension and wettability," *Ind. Eng. Chem. Res.* **57**, 371–379 (2018).
- T. B. Le, A. Striolo, and D. R. Cole, "Supercritical CO₂ effects on calcite wettability: A molecular perspective," *J. Phys. Chem. C* **124**, 18532–18543 (2020).
- L. C. Nielsen, I. C. Bourg, and G. Sposito, "Predicting CO₂-water interfacial tension under pressure and temperature conditions of geologic CO₂ storage," *Geochim. Cosmochim. Acta* **81**, 28–38 (2012).
- A. K. Narayanan Nair, M. F. Anwari Che Ruslan, M. L. Ramirez Hincapie, and S. Sun, "Bulk and interfacial properties of brine or alkane in the presence of carbon dioxide, methane, and their mixture," *Ind. Eng. Chem. Res.* **61**, 5016–5029 (2022).

- ²⁹P. Naeiji, T. K. Woo, S. Alavi, and R. Ohmura, "Molecular dynamics simulations of interfacial properties of the CO₂-water and CO₂-CH₄-water systems," *J. Chem. Phys.* **153**, 044701 (2020).
- ³⁰X. Li, D. A. Ross, J. M. Trusler, G. C. Maitland, and E. S. Boek, "Molecular dynamics simulations of CO₂ and brine interfacial tension at high temperatures and pressures," *J. Phys. Chem. B* **117**, 5647–5652 (2013).
- ³¹H. Jiang, I. G. Economou, and A. Z. Panagiotopoulos, "Molecular modeling of thermodynamic and transport properties for CO₂ and aqueous brines," *Acc. Chem. Res.* **50**, 751–758 (2017).
- ³²L. F. Franco, M. Castier, and I. G. Economou, "Anisotropic parallel self-diffusion coefficients near the calcite surface: A molecular dynamics study," *J. Chem. Phys.* **145**, 084702 (2016).
- ³³J. Sun, C. Chen, Y. Zhang, W. Li, and Y. Song, "Competitive adsorption characteristics based on partial pressure and adsorption mechanism of CO₂/CH₄ mixture in shale pores," *Chem. Eng. J.* **430**, 133172 (2022).
- ³⁴S. Mohammed, A. K. Sunkara, C. E. Walike, and G. Gadikota, "The role of surface hydrophobicity on the structure and dynamics of CO₂ and CH₄ confined in silica nanopores," *Front. Clim.* **3**, 713708 (2021).
- ³⁵T. Le, A. Striolo, and D. R. Cole, "CO₂-C₄H₁₀ mixtures simulated in silica slit pores: Relation between structure and dynamics," *J. Phys. Chem. C* **119**, 15274–15284 (2015).
- ³⁶J. Qian, H. Wu, and F. Wang, "Molecular geometry effect on gas transport through nanochannels: Beyond Knudsen theory," *Appl. Surf. Sci.* **611**, 155613 (2023).
- ³⁷H. Heinz, T.-J. Lin, R. Kishore Mishra, and F. Emami, "Thermodynamically consistent force fields for the assembly of inorganic, organic, and biological nanostructures: The interface force field," *Langmuir* **29**, 1754–1765 (2013).
- ³⁸F. S. Emami, V. Puddu, R. J. Berry, V. Varshney, S. V. Patwardhan, C. C. Perry, and H. Heinz, "Force field and a surface model database for silica to simulate interfacial properties in atomic resolution," *Chem. Mater.* **26**, 2647–2658 (2014).
- ³⁹S. Wang, K. Hou, and H. Heinz, "Accurate and compatible force fields for molecular oxygen, nitrogen, and hydrogen to simulate gases, electrolytes, and heterogeneous interfaces," *J. Chem. Theory Comput.* **17**, 5198–5213 (2021).
- ⁴⁰J. J. Potoff and J. I. Siepmann, "Vapor-liquid equilibria of mixtures containing alkanes, carbon dioxide, and nitrogen," *AIChE J.* **47**, 1676–1682 (2001).
- ⁴¹W. L. Jorgensen, D. S. Maxwell, and J. Tirado-Rives, "Development and testing of the OPLS all-atom force field on conformational energetics and properties of organic liquids," *J. Am. Chem. Soc.* **118**, 11225–11236 (1996).
- ⁴²J. L. Abascal and C. Vega, "A general purpose model for the condensed phases of water: TIP4P/2005," *J. Chem. Phys.* **123**, 234505 (2005).
- ⁴³C. Chen, W. Hu, W. Li, and Y. Song, "Model comparison of the CH₄/CO₂/water system in predicting dynamic and interfacial properties," *J. Chem. Eng. Data* **64**, 2464–2474 (2019).
- ⁴⁴W. van Rooijen, P. Habibi, K. Xu, P. Dey, T. Vlugt, H. Hajibeygi, and O. Moulton, "Interfacial tensions, solubilities, and transport properties of the H₂/H₂O/NaCl system: A molecular simulation study," *J. Chem. Eng. Data* (published online 2023).
- ⁴⁵Y. Yang, A. K. N. Nair, W. Zhu, S. Sang, and S. Sun, "Molecular perspectives of interfacial properties of the hydrogen+water mixture in contact with silica or kerogen," *J. Mol. Liquids* **385**, 122337 (2023).
- ⁴⁶S. Plimpton, "Fast parallel algorithms for short-range molecular dynamics," *J. Comput. Phys.* **117**, 1–19 (1995).
- ⁴⁷A. Stukowski, "Visualization and analysis of atomistic simulation data with OVITO—the open visualization tool," *Modell. Simul. Mater. Sci. Eng.* **18**, 015012 (2009).
- ⁴⁸L. Martínez, R. Andrade, E. G. Birgin, and J. M. Martínez, "PACKMOL: A package for building initial configurations for molecular dynamics simulations," *J. Comput. Chem.* **30**, 2157–2164 (2009).
- ⁴⁹J. Zhou, J. Zhang, J. Yang, Z. Jin, and K. H. Luo, "Mechanisms for kerogen wettability transition from water-wet to CO₂-wet: Implications for CO₂ sequestration," *Chem. Eng. J.* **428**, 132020 (2022).
- ⁵⁰C. Bistafa, D. Surbly, H. Kusudo, and Y. Yamaguchi, "Water on hydroxylated silica surfaces: Work of adhesion, interfacial entropy, and droplet wetting," *J. Chem. Phys.* **155**, 064703 (2021).
- ⁵¹M. S. Green, "Markoff random processes and the statistical mechanics of time-dependent phenomena. II. Irreversible processes in fluids," *J. Chem. Phys.* **22**, 398–413 (1954).
- ⁵²R. Kubo, "Statistical-mechanical theory of irreversible processes. I. General theory and simple applications to magnetic and conduction problems," *J. Phys. Soc. Jpn.* **12**, 570–586 (1957).
- ⁵³X. Nie, Z. Du, L. Zhao, S. Deng, and Y. Zhang, "Molecular dynamics study on transport properties of supercritical working fluids: Literature review and case study," *Appl. Energy* **250**, 63–80 (2019).
- ⁵⁴F. Feldmann, B. Hagemann, L. Ganzer, and M. Panfilov, "Numerical simulation of hydrodynamic and gas mixing processes in underground hydrogen storages," *Environ. Earth Sci.* **75**, 1165 (2016).
- ⁵⁵A. Silvestri, E. Ataman, A. Budi, S. Stipp, J. D. Gale, and P. Raiteri, "Wetting properties of the CO₂-water-calcite system via molecular simulations: Shape and size effects," *Langmuir* **35**, 16669–16678 (2019).
- ⁵⁶B. Shi and V. K. Dhir, "Molecular dynamics simulation of the contact angle of liquids on solid surfaces," *J. Chem. Phys.* **130**, 034705 (2009).
- ⁵⁷S. Iglauer, M. Ali, and A. Keshavarz, "Hydrogen wettability of sandstone reservoirs: Implications for hydrogen geo-storage," *Geophys. Res. Lett.* **48**, e2020GL090814, <https://doi.org/10.1029/2020GL090814> (2021).
- ⁵⁸A. Z. Al-Yaseri, M. Lebedev, A. Barifcani, and S. Iglauer, "Receding and advancing (CO₂+brine+quartz) contact angles as a function of pressure, temperature, surface roughness, salt type and salinity," *J. Chem. Thermodyn.* **93**, 416–423 (2016).
- ⁵⁹B. Pan, F. Jones, Z. Huang, Y. Yang, Y. Li, S. H. Hejazi, and S. Iglauer, "Methane (CH₄) wettability of clay-coated quartz at reservoir conditions," *Energy Fuels* **33**, 788–795 (2019).
- ⁶⁰S. Iglauer, "CO₂-water-rock wettability: Variability, influencing factors, and implications for CO₂ geostorage," *Acc. Chem. Res.* **50**, 1134–1142 (2017).
- ⁶¹M. Arif, A. Z. Al-Yaseri, A. Barifcani, M. Lebedev, and S. Iglauer, "Impact of pressure and temperature on CO₂-brine-mica contact angles and CO₂-brine interfacial tension: Implications for carbon geo-sequestration," *J. Colloid Interface Sci.* **462**, 208–215 (2016).
- ⁶²A. Z. Al-Yaseri, H. Roshan, M. Lebedev, A. Barifcani, and S. Iglauer, "Dependence of quartz wettability on fluid density," *Geophys. Res. Lett.* **43**, 3771–3776, <https://doi.org/10.1002/2016GL068278> (2016).
- ⁶³B. Pan, Y. Li, L. Xie, X. Wang, Q. He, Y. Li, S. H. Hejazi, and S. Iglauer, "Role of fluid density on quartz wettability," *J. Pet. Sci. Eng.* **172**, 511–516 (2019).
- ⁶⁴L. Hashemi, M. Boon, W. Glerum, R. Farajzadeh, and H. Hajibeygi, "A comparative study for H₂-CH₄ mixture wettability in sandstone porous rocks relevant to underground hydrogen storage," *Adv. Water Resour.* **163**, 104165 (2022).
- ⁶⁵V. Mirchi, M. Dejam, and V. Alvarado, "Interfacial tension and contact angle measurements for hydrogen-methane mixtures/brine/oil-wet rocks at reservoir conditions," *Int. J. Hydrogen Energy* **47**, 34963–34975 (2022).
- ⁶⁶M. Arif, W. Wülling, A. S. Adila, A. Raza, M. Mahmoud, and S. Iglauer, "Shale wettability and influencing factors: A statistical investigation," *Energy Fuels* **36**, 12651–12662 (2022).
- ⁶⁷A. Al-Yaseri, S. Abdel-Azeim, and J. Al-Hamad, "Wettability of water-H₂-quartz and water-H₂-calcite experiment and molecular dynamics simulations: Critical assessment," *Int. J. Hydrogen Energy* **48**, 34897 (2023).
- ⁶⁸S. Abdel-Azeim, A. Al-Yaseri, K. Norrman, P. Patil, A. Qasim, and A. Yousef, "Wettability of caprock-H₂-water: Insights from molecular dynamic simulations and sessile-drop experiment," *Energy Fuels* **37**, 19348 (2023).
- ⁶⁹G. Javanbakht, M. Sedghi, W. Welch, and L. Goual, "Molecular dynamics simulations of CO₂/water/quartz interfacial properties: Impact of CO₂ dissolution in water," *Langmuir* **31**, 5812–5819 (2015).
- ⁷⁰C. M. Tenney and R. T. Cygan, "Molecular simulation of carbon dioxide, brine, and clay mineral interactions and determination of contact angles," *Environ. Sci. Technol.* **48**, 2035–2042 (2014).
- ⁷¹A. Liu and S. Liu, "Hydrogen sorption and diffusion in coals: Implications for hydrogen geo-storage," *Appl. Energy* **334**, 120746 (2023).
- ⁷²J. Ji, L. Zhao, L. Tao, and S. Lin, "Molecular Gibbs surface excess and CO₂-hydrate density determine the strong temperature- and pressure-dependent supercritical CO₂-brine interfacial tension," *J. Phys. Chem. B* **121**, 6200–6207 (2017).

- ⁷³M. Hosseini, J. Fahimpour, M. Ali, A. Keshavarz, and S. Iglauer, "H₂-brine interfacial tension as a function of salinity, temperature, and pressure; implications for hydrogen geo-storage," *J. Pet. Sci. Eng.* **213**, 110441 (2022).
- ⁷⁴Y. F. Chow, G. C. Maitland, and J. M. Trusler, "Interfacial tensions of (H₂O+H₂) and (H₂O+CO₂+H₂) systems at temperatures of (298–448) K and pressures up to 45 MPa," *Fluid Phase Equilib.* **475**, 37–44 (2018).
- ⁷⁵P. Chiquet, J.-L. Daridon, D. Broseta, and S. Thibeau, "CO₂/water interfacial tensions under pressure and temperature conditions of CO₂ geological storage," *Energy Convers. Manage.* **48**, 736–744 (2007).
- ⁷⁶A. Georgiadis, G. Maitland, J. M. Trusler, and A. Bismarck, "Interfacial tension measurements of the (H₂O+CO₂) system at elevated pressures and temperatures," *J. Chem. Eng. Data* **55**, 4168–4175 (2010).
- ⁷⁷Y. Liu, H. A. Li, and R. Okuno, "Measurements and modeling of interfacial tension for CO₂/CH₄/brine systems under reservoir conditions," *Ind. Eng. Chem. Res.* **55**, 12358–12375 (2016).
- ⁷⁸K. Kashefi, L. M. Pereira, A. Chapoy, R. Burgass, and B. Tohidi, "Measurement and modelling of interfacial tension in methane/water and methane/brine systems at reservoir conditions," *Fluid Phase Equilib.* **409**, 301–311 (2016).
- ⁷⁹L. Zhao, S. Lin, J. D. Mendenhall, P. K. Yuet, and D. Blankschtein, "Molecular dynamics investigation of the various atomic force contributions to the interfacial tension at the supercritical CO₂-water interface," *J. Phys. Chem. B* **115**, 6076–6087 (2011).
- ⁸⁰Z. Sun, B. Huang, S. Wang, K. Wu, H. Li, and Y. Wu, "Hydrogen adsorption in nanopores: Molecule-wall interaction mechanism," *Int. J. Hydrogen Energy* **48**, 33496 (2023).
- ⁸¹G. Wu, B. Huang, L. Cheng, J. Luan, R. Zhang, Z. Chen, C. Zeng, and Z. Sun, "CO₂ storage behavior in nanopores: Implications for CO₂ sequestration in ultra-tight geological formations," *Ind. Eng. Chem. Res.* **62**, 13677–13686 (2023).
- ⁸²R. R. Ratnakar and B. Dindoruk, "The role of diffusivity in oil and gas industries: Fundamentals, measurement, and correlative techniques," *Processes* **10**, 1194 (2022).
- ⁸³H. Zhong, S. Lai, J. Wang, W. Qiu, H.-D. Lüdemann, and L. Chen, "Molecular dynamics simulation of transport and structural properties of CO₂ using different molecular models," *J. Chem. Eng. Data* **60**, 2188–2196 (2015).
- ⁸⁴K. Ghosh and C. Krishnamurthy, "Soft-wall induced structure and dynamics of partially confined supercritical fluids," *J. Chem. Phys.* **150**, 111102 (2019).
- ⁸⁵G. J. Wang and N. G. Hadjiconstantinou, "Layered fluid structure and anomalous diffusion under nanoconfinement," *Langmuir* **34**, 6976–6982 (2018).
- ⁸⁶C. Chen, W. Hu, J. Sun, W. Li, and Y. Song, "CH₄ adsorption and diffusion in shale pores from molecular simulation and a model for CH₄ adsorption in shale matrix," *Int. J. Heat Mass Transfer* **141**, 367–378 (2019).
- ⁸⁷C. Cheng (2023). "cc_gas-liquid-solid," figshare. <https://doi.org/10.6084/m9.figshare.24438541.v1>